POLITECNICO DI TORINO
Repository ISTITUZIONALE

Sector Mode Assembling Reduction Technique for High-Fidelity Blisk Models with Geometry Mistuning

Original
Sector Mode Assembling Reduction Technique for High-Fidelity Blisk Models with Geometry Mistuning / Zhou, B., Zhao, J., Ye, N., Berruti, T.M.. - In: AIAA JOURNAL. - ISSN 0001-1452. - ELETTRONICO. - 61:1(2023), pp. 406-415. [10.2514/1.J062248]

Availability:
This version is available at: 11583/2974310 since: 2023-01-03T12:59:20Z

Publisher:
AIAA International

Published
DOI:10.2514/1.J062248

Terms of use:

This article is made available under terms and conditions as specified in the corresponding bibliographic description in the repository

Publisher copyright
AIAA preprint/submitted version e/o postprint/Author's Accepted Manuscript

© AIAA. Sector Mode Assembling Reduction Technique for High-Fidelity Blisk Models with Geometry Mistuning / Zhou, B.; Zhao, J.; Ye, N.; Berruti, T. M. published in : AIAA JOURNAL, 2023, 61, 1, 406-415, http://dx.doi.org/10.2514/1.J062248.

(Article begins on next page)

29 November 2026

Sector Mode Assembling Reduction Technique for High Fidelity Blisk Models Constructed upon Measured Geometry

Biao Zhou, * Jingchao Zhao † Nan Ye ‡
Nanjing University of Aeronautics and Astronautics, Nanjing, 210016, China

Teresa M. Berruti §
Politecnico di Torino, Torino, 10129, Italy

Blade mistuning in blisks arises primarily from the scatters of blade geometry profiles caused by manufacturing tolerance, in-service wear, blade repairs, etc. There is a recent trend to capture the blade-to-blade geometry variances through precise geometry measurements by a 3D optical scanning system in order to obtain an improved blade geometric mistuning evaluation capability. However, this usually leads to prohibitive computational costs due to the large-scale, high fidelity industrial blisk finite element models. This paper develops an original model reduction approach, "Sector Mode Assembling Reduction Technique" (SMART), specifically for the high fidelity blisk model fully mistuned by blade geometric variances, with either topologically compatible or incompatible blade meshes. The basic idea of SMART is to construct the sector-level reduction mode basis by strategically assembling the truncated cyclic modes independently computed for each "isolated" sector with assumed cyclic symmetry at the sector interfaces. Benefiting from the block structure of the SMART mode basis, the reduced-order models are derived by a series of sector-level projections with a relatively low memory requirement and computational cost. Another hidden benefit is that the SMART approach enables efficient structural modification predictions of the global blisk modes since only the modes of the sectors undergoing blade modification needs to be re-evaluated and replaced in the SMART mode basis. The SMART approach is applied into a high fidelity "As-Measured Model" of a blended blisk, constructed upon the geometry measurement by the state-of-the-art 3D optical scanning technology. It is fully demonstrated that the reduced-order model derived by SMART, featured by a minimal size, is able to reproduce the dynamics of the full-order as-measured blisk model with high accuracy.

Nomenclature

*Associate Professor, College of Energy and Power Engineering, 29 Yudao St., biao.zhou@nuaa.edu.cn.
†Master student, College of Energy and Power Engineering, 29 Yudao St., jc.zhao@nuaa.edu.cn.
‡Assistant Professor, College of Mechanical and Electrical Engineering, 29 Yudao St., yen@nuaa.edu.cn.
§Professor, Dipartimento di Ingegneria Meccanica e Aerospaziale, Corso Duca degli Abruzzi 24, teresa.berruti@polito.it.

$\mathbf{f}$ = full-blisk forcing vector in the integral form

f = blade-alone frequency

$\mathbf{K}$ = full-blisk stiffness matrix in the integral form

$\mathbf{M}$ = full-blisk mass matrix in the integral form

$\bar{\mathbf{M}}$ = full-blisk mass matrix in the uncoupled form

$\mathbf{E}$ = transformation matrix for the system matrix in the integral/uncoupled form

$\mathbf{I}$ = identity matrix

N = node of a finite element model

$\mathbf{T}(\alpha)$ = complex transformation matrix

$\mathbf{T}_{\gamma,j}$ = interface mode transformation matrix for the jth sector

$\vec{h}$ = node deformation vector

n = number of sectors

n_m = number of retained cyclic modes

n_s = number of different geometrically mistuned sector types

$\mathbf{q}$ = generalized coordinates

v = vertex in the point cloud

$\mathbf{x}$ = full-blisk displacement in the integral form

$\bar{\mathbf{x}}$ = full-blisk displacement in the uncoupled form

α = fundamental interblade phase angle

${}^{f}\delta$ = frequency mistuning pattern

ϵ_{r} = relative approximation error

γ = structural damping ratio

$\mathbf{\Phi}$ = full blisk modes in the integral form

$\bar{\mathbf{\Phi}}$ = full blisk modes in the uncoupled form

ω = frequency

Subscripts

H = high cyclic interface degrees of freedom

I = interior degrees of freedom

L = low cyclic interface degrees of freedom

j = generic variable

red = reduced system

Γ = interface degrees of freedom

Superscripts

h = harmonic index

I. Introduction

Blade integrated disks (blisks) comprise blades and a rotor disk in a single, integrally manufactured part. Extensively used in the fan/compressor sections, blisks substantially contribute to the improved aeroengine performance, driving efficiency and reduced engine weight. However, compared with the traditional inserted-blade designs, blisks are more susceptible to excessive blade vibrations due to the inevitable blade mistuning, plus a low structural damping level in the absence of blade-disk contact interfaces. Blade mistuning in blisks arises primarily from the intrinsic scatters of blade geometry profiles caused by manufacturing tolerance, in-service wear, geometry modification by blade blend repair technique, etc. Hence, the accurate modeling and dynamic analysis of geometrically mistuned blisks has been a long-standing issue in both the academic and industrial community [1–4].

More and more research works over the past decade have attempted to capture and quantify the small blade geometry variances by taking advantage of state-of-the-art 3D optical geometry measurement systems [5–7]. The high-resolution measurement data precisely representing the blade geometries, can be used to update an existing "seed" blisk finite element model (FEM). This is to create high-fidelity FEMs [8], or the so-called "as-manufactured model" for the real blisks with part-to-part geometry variations [9]. An admirable benefit of these high-fidelity blisk FEMs is that they can fully account for the blade geometric mistuning effect, i.e., the variations of both the blade frequencies and mode shapes due to the blade geometry variances. The latter, in particular, is typically absent in the traditional frequency-mistuning modeling approaches.

Experimental evidences reveal that the as-manufactured models give rise to improved blade mistuning evaluation capability for the newly manufactured blisks upon entry into service, with small intrinsic blade geometric variances [10]. These high-fidelity models have been also utilized for determining the sensor locations in an optimal sense [11, 12], more accurate fluid dynamic simulations [13], etc. More recently, the concept of "as-manufactured model" has been extended in a single blade [14] and a full blisk [15] undergoing blend repairs, respectively. All these research efforts align with the Digital Twin philosophy that the digital representations of the real aeroengine parts, converted from the precise geometry measurement data, enable to evaluate and monitor the products' performance through the life-cycle in an effective way.

The promising as-manufactured modeling technique also gives a strong incentive to develop efficient model reduction techniques specifically tailored for the high-fidelity blisk models fully mistuned by blade geometric variances. This relies on the observation that the blisk FEMs built upon the precisely measured geometry, require a high mesh density to fully capture the frequency/mode variations due to blade geometric variances [16]. Such a high-fidelity FEM for

a real industrial blisk can contain up to several million degrees of freedom (DOFs). This raises concerns over the computational efficiency to perform further structural analyses based on the full-order as-manufactured models. Apart from the prohibitive computational time consumption, the major bottleneck is attributed to the high memory required to run the large scale, full blisk simulations.

There exist numerous well-developed, efficient model reduction methods for blisks with small stiffness mistuning [17], or in some other cases, part of the blades are further mistuned by geometric modifications [18–21]. However, there are a quite limited number of options applicable to the blisks fully mistuned by blade geometric variances. These reduction techniques can be generally categorized into the the system-mode-based methods and component-mode-based methods.

The component-mode-based methods stem from the technique of component mode synthesis (CMS). They are featured by a substructuring step, by which the full-order blisk model is partitioned into either blade/disk components [22] or sector components [23, 24]. The dynamic substructuring therefore allows a straightforward integration of both small intrinsic blade geometric variances and large blade geometry modification, e.g., by blend repairs [25]. The individual component normal/constraint modes are computed independently, and then assembled systematically through the compatibility constraints at the component interfaces as the reduction mode basis for the full blisk. It should be pointed out that the resultant reduced-order models (ROMs) usually suffer a relatively large size, since a large number of component interface DOFs are retained in the ROM. Although the interface DOFs can be reduced through *a posteriori* secondary modal analysis [26], it still requires high computational cost that scales heavily with the number of the constraint modes. An appealing improvement, referred to as the Orthogonal Polynomial Series method, was recently proposed to efficiently calculate the constraint mode matrix in a reduced form, meanwhile significantly eliminate the interface DOFs in the final ROM [27].

The system-mode-based methods are generally considered more computational efficient than the component-mode-based methods. No substructuring is required. The reduction mode basis is constructed by gathering the truncated cyclic modes of the different geometrically mistuned sectors [28–30], expanded to the full blisk. A prerequisite of the system-mode-based methods is that the geometrically mistuned blisks should have topologically compatible meshes among all the blades. In other words, the geometrically mistuned sectors are supposed to have substantially similar topology and exactly the same FE node numbers as the nominal tuned sectors. This limits their applications since the blades experiencing large geometric modifications, e.g., blade damages or repairs with material loss, tend to produce modified blade meshes incompatible with the blades with small geometric variances [31].

This paper is dedicate to an original model reduction approach, named as “Sector Mode Assembling Reduction Technique”(SMART), for geometrically mistuned blisk model with either compatible or incompatible blade meshes. It starts from substructuring the full-order blisk model into physically “isolated” sectors. Physical displacement of each sector, with a unique blade geometric profile, can be independently approximated by a set of truncated cyclic modes of

its own. Subsequently the cyclic modes for all the separate sectors are strategically assembled to form the reduction mode basis for the full blisk.

The SMART approach is anticipated to offer superior performance over the aforementioned model reduction methods for the blisk fully mistuned by geometric variances. On the one hand, benefiting from the substructuring step, the SMART approach is able to tackle the small blade geometric mistuning with compatible meshes, as well as the large blade geometric modification accompanied by incompatible meshes. This puts the SMART approach at an advantage over the existent system-mode-based methods. On the other hand, the SMART approach does not require to compute the constraint modes for each sector and the interface DOFs are excluded in the ROM. It is therefore supposed to significantly outperform the component-mode-based methods in terms of computational efficiency.

This paper will be organized as follows: the framework of the proposed SMART approach is developed in Sec. II. This novel reduction technique will be applied to a high-fidelity blisk model with incompatible blade meshes due to a single blend repair, which was recently constructed upon the measured blade geometries by 3D optical scanning system [15]. Performance of the SMART approach will be fully addressed by comparison with the full-order FE model analysis results in Sec. III.

II. Methodology

Let us consider a representative full-order FEM of a geometrically mistuned blisk with n-sector in Fig. 1. It comprises a blended sector and the remaining pristine sectors with small geometric mistuning. The disk part features cyclic symmetry. Due to the material loss, the blended blade mesh is topologically incompatible with the pristine blades. The equation of motion can be written in the frequency-domain in terms of the full blisk displacement $\mathbf{x}$ in the global cylindrical coordinates system:

$$\left[(1+i\gamma)\mathbf{K}-\omega^2\mathbf{M}\right]\mathbf{x}=\mathbf{f} \tag{1}$$

where $\mathbf{K}$ and $\mathbf{M}$ are full-blisk stiffness and mass matrix, respectively; γ is the structural damping ratio and $i^2=-1$; $\mathbf{f}$ is the amplitude of external forcing exerted onto the blades.

In general, the model reduction technique aims to seek a reduction mode basis $\mathbf{\Phi}$, onto which the displacement $\mathbf{x}$ of the full-order blisk FEM can be projected as

$$\mathbf{x}=\mathbf{\Phi q} \tag{2}$$

where $\mathbf{q}$ denotes the generalized coordinates.

Since the number of retained modes (the column size of $\mathbf{\Phi}$) is much less than the total DOFs of the full blisk FEM (the row size of $\mathbf{\Phi}$), the following reduced system matrices and forcing term can be theoretically derived:

$$\mathbf{M}_{\text{red}}=\mathbf{\Phi}^{\text{T}}\mathbf{M}\mathbf{\Phi},\quad \mathbf{K}_{\text{red}}=\mathbf{\Phi}^{\text{T}}\mathbf{K}\mathbf{\Phi},\quad \mathbf{f}_{\text{red}}=\mathbf{\Phi}^{\text{T}}\mathbf{f} \tag{3}$$

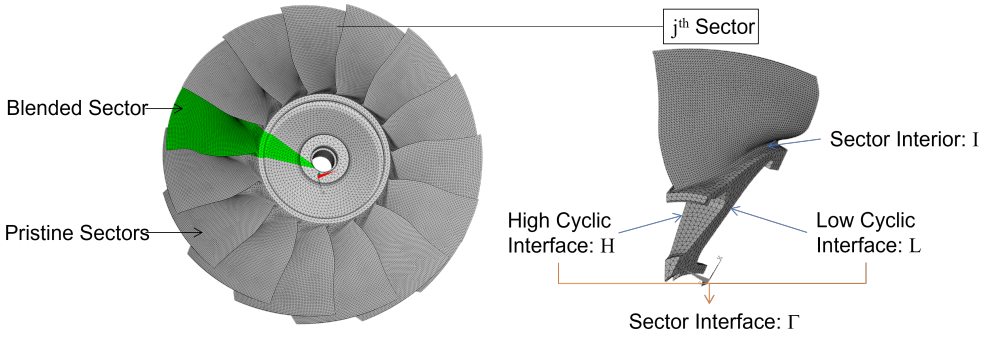

Fig. 1 A full-order blisk FEM (left) and index notation (right)

The above reduced quantities constitute a reduced-order model, whose size is governed by the number of retained modes in $\mathbf{\Phi}$. It should be reminded that Eq. (2)~(3) represent a system-level projection as the $\mathbf{\Phi}$ stands for the full blisk modes. For the large-scale industrial blisk FEMs, the system-level projection usually requires a large amount of memory since it implies to manage the full-blisk system matrix and modes simultaneously. For this reason, the projection process is practically implemented by sector-level computations.

A. System-level Projection by Sector-level Computations

According to the notation for the "isolated" j^{th} sector in Fig. 1 ($j = 1, 2, \cdots, n$), the sector-level displacement vector, modes and mass matrix in the local cylindrical coordinate system associated with each sector can be rearranged as follows:

$$\bar{\mathbf{x}}_j = \begin{bmatrix} \mathbf{x}_{j,\mathrm{L}} \\ \mathbf{x}_{j,\mathrm{I}} \\ \mathbf{x}_{j,\mathrm{H}} \end{bmatrix}, \quad \bar{\mathbf{\Phi}}_j = \begin{bmatrix} \mathbf{\Phi}_{j,\mathrm{L}} \\ \mathbf{\Phi}_{j,\mathrm{I}} \\ \mathbf{\Phi}_{j,\mathrm{H}} \end{bmatrix}, \quad \bar{\mathbf{M}}_j = \begin{bmatrix} \mathbf{M}_{j,\mathrm{LL}} & \mathbf{M}_{j,\mathrm{LI}} & \mathbf{M}_{j,\mathrm{LH}} \\ \mathbf{M}_{j,\mathrm{IL}} & \mathbf{M}_{j,\mathrm{II}} & \mathbf{M}_{j,\mathrm{IH}} \\ \mathbf{M}_{j,\mathrm{HL}} & \mathbf{M}_{j,\mathrm{HI}} & \mathbf{M}_{j,\mathrm{HH}} \end{bmatrix} \tag{4}$$

where the "bar" notation indicates sector-level quantities throughout this paper. These quantities include the DOFs related to both the low and high cyclic interfaces of each sector. The sector-level stiffness matrix $\bar{\mathbf{K}}_j$ and forcing vector $\bar{\mathbf{f}}_j$ are rearranged in exactly the same manner. It should be pointed out that the size of $\mathbf{x}_{j,\mathrm{I}}$ corresponding to the physical DOFs of the sector interior nodes could vary with j due to the incompatible blade meshes.

By gathering the sector-level mass matrices $\bar{\mathbf{M}}_j$ and the modes $\bar{\mathbf{\Phi}}_j$ for all the n "isolated" sectors, one obtains the

full-blisk mass matrix and modes in the uncoupled form:

$$\bar{\mathbf{M}} = \begin{bmatrix} \bar{\mathbf{M}}_1 & & & & \\ & \ddots & & & \\ & & \bar{\mathbf{M}}_j & & \\ & & & \ddots & \\ & & & & \bar{\mathbf{M}}_n \end{bmatrix}, \quad \bar{\mathbf{\Phi}} = \begin{bmatrix} \bar{\mathbf{\Phi}}_1 \\ \vdots \\ \bar{\mathbf{\Phi}}_j \\ \vdots \\ \bar{\mathbf{\Phi}}_n \end{bmatrix} \tag{5}$$

The full-blisk mass matrix $\bar{\mathbf{M}}$ in the uncoupled form is related to the integral form $\mathbf{M}$ in Eq. (1) by the following transform [20]:

$$\mathbf{M} = \mathbf{E}^{\mathrm{T}} \bar{\mathbf{M}} \mathbf{E} \tag{6}$$

where the transformation matrix $\mathbf{E}$ is defined as

$$\mathbf{E} = \begin{bmatrix} \mathbf{E}_{1,a} & \mathbf{E}_{1,b} & \mathbf{0} & \cdots & \mathbf{0} \\ \mathbf{0} & \mathbf{E}_{2,a} & \mathbf{E}_{2,b} & \cdots & \mathbf{0} \\ \vdots & \vdots & \ddots & \ddots & \mathbf{0} \\ \mathbf{E}_{n,b} & \mathbf{0} & \mathbf{0} & \cdots & \mathbf{E}_{n,a} \end{bmatrix} \tag{7}$$

The submatrices in $\mathbf{E}$ read

$$\mathbf{E}_{j,a} = \begin{bmatrix} \mathbf{I}_{j,\mathrm{L}} & \mathbf{0} \\ \mathbf{0} & \mathbf{I}_{j,\mathrm{I}} \\ \mathbf{0} & \mathbf{0} \end{bmatrix}, \quad \mathbf{E}_{j,b} = \begin{bmatrix} \mathbf{0} & \mathbf{0} \\ \mathbf{0} & \mathbf{0} \\ \mathbf{I}_{j,\mathrm{H}} & \mathbf{0} \end{bmatrix}, \quad j = 1, 2, \cdots, n \tag{8}$$

where $\mathbf{I}_{j,\mathrm{I}}$, $\mathbf{I}_{j,\mathrm{L}}$ and $\mathbf{I}_{j,\mathrm{H}}$ are identity matrices of which the sizes are in accordance with the number of DOFs for the interior nodes, low and high cyclic interface nodes respectively, in the jth sector. $\mathbf{E}$ is not necessarily a circulant matrix because $\mathbf{I}_{j,\mathrm{I}}$ for the blended sector differs from that of the pristine sectors in the size.

Similarly, one can establish the link between the full-blisk modes $\bar{\mathbf{\Phi}}$ in the uncoupled form and the modes $\mathbf{\Phi}$ in the integral form as

$$\bar{\mathbf{\Phi}} = \mathbf{E}\mathbf{\Phi} \tag{9}$$

It should be addressed that both Eq. (6) and Eq. (9) describe exact transforms and there is no approximation inside. The full-blisk matrix and modes in the uncoupled/integral form are mutually equivalent in terms of representing the

physical quantities. By substituting Eq. (5) and Eq. (9) into Eq. (3), one can obtain the reduced mass matrix in an alternative way:

$$\begin{aligned}\mathbf{M}_{\text{red}} &= \boldsymbol{\Phi}^{\mathrm{T}}\mathbf{M}\boldsymbol{\Phi} = \boldsymbol{\Phi}^{\mathrm{T}}\left(\mathbf{E}^{\mathrm{T}}\bar{\mathbf{M}}\mathbf{E}\right)\boldsymbol{\Phi} = \left(\mathbf{E}\boldsymbol{\Phi}\right)^{\mathrm{T}}\bar{\mathbf{M}}\left(\mathbf{E}\boldsymbol{\Phi}\right) = \bar{\boldsymbol{\Phi}}^{\mathrm{T}}\bar{\mathbf{M}}\bar{\boldsymbol{\Phi}} \\ &= \sum_{j=1}^{n}\bar{\boldsymbol{\Phi}}_j^{\mathrm{T}}\bar{\mathbf{M}}_j\bar{\boldsymbol{\Phi}}_j \end{aligned} \tag{10}$$

Eq. (10) converts the system-level projection into the sum of a series of matrix products over the sector-level matrix and modes. The other reduced quantities in Eq. (3) can be treated in the similar manner. As a consequence, the computationally expensive system-level projections can be efficiently realized by the sector-level computations with a relatively low computational cost and memory requirement.

A new reduction approach called "Sector Mode Assembling Reduction Technique" (SMART), is hereby proposed to construct a sector-level reduction mode basis $\bar{\boldsymbol{\Phi}}_j$, as involved in the sector-level computations expressed by Eq. (10).

B. Sector Mode Assembling Reduction Technique

The basic idea of SMART is to construct the reduction mode basis for the full-order blisk FEM by strategically assembling the truncated cyclic modes for each "isolated" sector. This approach will be elaborated below as a two-step scheme.

1. Sector-level mode projection

The SMART approach proposes to individually project the physical displacement of the jth "isolated" sector, including a unique blade geometry, onto a set of truncated cyclic modes, which are obtained on the same sector with assumed cyclic boundary constraints, and expanded to only this sector. This sector-level mode projection can be expressed as:

$$\bar{\mathbf{x}}_j = \begin{bmatrix}\mathbf{x}_{j,\mathrm{L}}\\ \mathbf{x}_{j,\mathrm{I}}\\ \mathbf{x}_{j,\mathrm{H}}\end{bmatrix} = \begin{bmatrix}\boldsymbol{\Phi}_{j,\mathrm{L}}\\ \boldsymbol{\Phi}_{j,\mathrm{I}}\\ \boldsymbol{\Phi}_{j,\mathrm{H}}\end{bmatrix}\cdot\mathbf{q}_j = \bar{\boldsymbol{\Phi}}_j\cdot\mathbf{q}_j, \quad j = 1, 2, \cdots, n \tag{11}$$

where $\mathbf{q}_j$ stands for the modal coordinates to be determined for the jth sector. $\bar{\boldsymbol{\Phi}}_j$ is the cyclic modes of a "tuned" blisk, truncated both modally and spatially at the jth sector. The physically non-existent "tuned" blisk carries n duplicated sectors identical with the jth sector. In practice, $\bar{\boldsymbol{\Phi}}_j$ can be readily obtained from a cyclic modal analysis, where the jth sector is treated as a reference sector with assumed cyclic symmetry at the sector interfaces.

For the sake of convenience, the cyclic modes $\bar{\boldsymbol{\Phi}}_j$ in Eq. (11) are considered in the complex-valued form. They are arranged as $\bar{\boldsymbol{\Phi}}_j = [\bar{\boldsymbol{\Phi}}_j^{(0)}, \bar{\boldsymbol{\Phi}}_j^{(1)}, \cdots, \bar{\boldsymbol{\Phi}}_j^{(h)}, \cdots]$, where $\bar{\boldsymbol{\Phi}}_j^{(h)}$ denotes the cyclic modes with the harmonic index h. Due to the nature of cyclic modes, a complex transformation matrix $\mathbf{T}(\alpha)$ can be constructed to link the modes at the low/high

cyclic interface DOFs in the jth sector as

$$\boldsymbol{\Phi}_{j,\mathrm{H}} = \boldsymbol{\Phi}_{j,\mathrm{L}} \cdot \mathbf{T}(\alpha) = \boldsymbol{\Phi}_{j,\mathrm{L}} \cdot \begin{bmatrix} \mathbf{I}_{n_m^{(0)}} & & & & \\ & e^{i\alpha} \otimes \mathbf{I}_{n_m^{(1)}} & & & \\ & & \ddots & & \\ & & & e^{ih\alpha} \otimes \mathbf{I}_{n_m^{(h)}} & \\ & & & & \ddots \end{bmatrix} \tag{12}$$

where $\alpha = 2\pi/n$ is the fundamental interblade phase angle; $\mathbf{I}_{n_m^{(h)}}$ is an identity matrix of the size $n_m^{(h)}$, which is the number of retained cyclic modes with the harmonic index h. As a matter of fact, Eq. (12) represents the assumed cyclic boundary constraints for the jth sector.

Furthermore, one can gather the modes at the low/high cyclic interface DOFs into the interface modes associated with the jth sector:

$$\boldsymbol{\Phi}_{j,\Gamma} = \begin{bmatrix} \boldsymbol{\Phi}_{j,\mathrm{L}} \\ \boldsymbol{\Phi}_{j,\mathrm{H}} \end{bmatrix} \tag{13}$$

At this point, an Interface Mode Transformation (IMT) is introduced as one of the cornerstones of the proposed SMART approach. This transformation holds for the blisks consist of only blade-to-blade physical/geometric variances. It relies on the assumption that the interface modes extracted from the cyclic modes for a reference sector with assumed cyclic symmetry, e.g., $\boldsymbol{\Phi}_{1,\Gamma}$, can be expressed as a linear combination of the interface modes $\boldsymbol{\Phi}_{j,\Gamma}$ of the jth sector, which is also considered in cyclic symmetry. A matrix representation of the IMT is formulated as

$$\boldsymbol{\Phi}_{j,\Gamma} \cdot \mathbf{T}_{\gamma,j} = \boldsymbol{\Phi}_{1,\Gamma}, \quad j = 2, 3, \cdots, n \tag{14}$$

where $\mathbf{T}_{\gamma,j}$, hereafter called "IMT matrix", denotes the transformation matrix for the jth sector. Note that any arbitrary sector other than the 1st sector can also be assigned as the reference sector for the interface mode transformation.

In essence, Eq. (14) exploits the fact that the disk part of the full blisk model still features cyclic symmetry. Hence, the modal deflections of the disk part in the two sets of cyclic modes for the 1st and j^{th} sector repectively, exhibit high similitude. For this reason, it is recommended to retain the same number of cyclic modes n_m in Eq. (11) for each individual sector such that the interface mode similitude in Eq. (14) can be achieved. In this condition, $\mathbf{T}_{\gamma,j}$, a fully populated matrix of the size $n_m \times n_m$ representing the connection between the two sets of interface modes, can be approximated as a least squares solution to Eq. (14). Notice that this does not require an intensive computational effort since the interface DOFs merely account for a small fraction of the total DOFs in each sector. The relative approximation

error can be evaluated in terms of matrix norms:

$$\epsilon_{\mathrm{r}} = \frac{\left\|\boldsymbol{\Phi}_{j,\Gamma} \cdot \mathbf{T}_{\gamma,j} - \boldsymbol{\Phi}_{1,\Gamma}\right\|_2}{\left\|\boldsymbol{\Phi}_{1,\Gamma}\right\|_2} \tag{15}$$

Magnitudes of the relative error ϵ_{r} are typically of the order $o(10^{-4})$. The appropriateness of the IMT as defined in Eq. (14) is therefore justified.

The IMT matrix further enables to transform the projection basis $\bar{\boldsymbol{\Phi}}_j$ into $\bar{\boldsymbol{\Phi}}_j^{\mathrm{IMT}}$ and the sector-level mode projection in Eq. (11) evolves into:

$$\bar{\mathbf{x}}_1 = \bar{\boldsymbol{\Phi}}_1^{\mathrm{IMT}} \cdot \mathbf{q}_1 = \bar{\boldsymbol{\Phi}}_1 \cdot \mathbf{q}_1 \tag{16}$$

$$\bar{\mathbf{x}}_j = \bar{\boldsymbol{\Phi}}_j^{\mathrm{IMT}} \cdot \mathbf{q}_j = \bar{\boldsymbol{\Phi}}_j \mathbf{T}_{\gamma,j} \cdot \mathbf{q}_j = \begin{bmatrix} \boldsymbol{\Phi}_{j,\mathrm{L}} \\ \boldsymbol{\Phi}_{j,\mathrm{I}} \\ \boldsymbol{\Phi}_{j,\mathrm{H}} \end{bmatrix} \cdot \mathbf{T}_{\gamma,j} \cdot \mathbf{q}_j = \begin{bmatrix} \boldsymbol{\Phi}_{1,\mathrm{L}} \\ \boldsymbol{\Phi}_{j,\mathrm{I}} \cdot \mathbf{T}_{\gamma,j} \\ \boldsymbol{\Phi}_{1,\mathrm{H}} \end{bmatrix} \cdot \mathbf{q}_j, \quad j = 2, 3, \cdots, n \tag{17}$$

It can be seen that for the reference sector 1, the cyclic mode basis in fact remains invariant in Eq. (16). While the cyclic mode basis for the remaining sectors is reshaped as $\bar{\boldsymbol{\Phi}}_j^{\mathrm{IMT}} = \bar{\boldsymbol{\Phi}}_j \mathbf{T}_{\gamma,j}$. This change of projection basis naturally holds since each column vector in $\bar{\boldsymbol{\Phi}}_j^{\mathrm{IMT}}$ is a linear superposition of the cyclic modes in the original basis $\bar{\boldsymbol{\Phi}}_j$. Most importantly, Eq. (17) shows that, through the IMT matrix $\mathbf{T}_{\gamma,j}$, the original cyclic mode basis $\bar{\boldsymbol{\Phi}}_j$ for each individual sector with a unique blade geometry, can be adapted into the form represented by $\bar{\boldsymbol{\Phi}}_j^{\mathrm{IMT}}$, such that it carries the same modal information at the disk interface DOFs as that of the reference sector 1. This gives a favorable condition for assembling the cyclic modes for the n "isolated" sectors in the next step.

2. Sector-level mode assembling

Note that the sector-level mode projection expressed in Eq. (16)-Eq. (17) is independently proceeded for each "isolated" sector. In order to generate the ROM for the full-order blisk, an admissible displacement field should be guaranteed at the physically coupled sector interfaces. This can be achieved by imposing the physical displacement compatibility condition at the common disk interface between the adjacent j^{th} and $(j+1)^{\mathrm{th}}$ sector:

$$\bar{\mathbf{x}}_{j,\mathrm{H}} = \bar{\mathbf{x}}_{j+1,\mathrm{L}}, \quad j = 1, 2, \cdots, n \tag{18}$$

where the right-hand side should be replaced by $\bar{\mathbf{x}}_{1,\mathrm{L}}$ if $j = n$.

The physical displacement at the interface DOFs of the two adjacent sectors can be extracted from Eq. (16) ∼

Eq. (17) respectively. Accordingly, Eq. (18) can be rewritten as

$$\mathbf{\Phi}_{1,\mathrm{H}} \cdot \mathbf{q}_j = \mathbf{\Phi}_{1,\mathrm{L}} \cdot \mathbf{q}_{j+1} \tag{19}$$

Let us recall the complex matrix $\mathbf{T}(\alpha)$ bridging the low/high cyclic interface modes for each individual sector. Substituting Eq. (12) into Eq. (19) leads to the following transform, which represents the dependence of the two sets of modal coordinates:

$$\mathbf{T}(\alpha) \cdot \mathbf{q}_j = \mathbf{q}_{j+1} \tag{20}$$

Consider $\mathbf{q}_1$ for the reference sector as the independent modal coordinates. The propagation relation in Eq. (20) allows to determine the modal coordinates for the remaining sectors in a deductive way:

$$\begin{aligned}
\mathbf{q}_1 &= \mathbf{q}_1 \\
\mathbf{q}_2 &= \mathbf{T}(\alpha) \cdot \mathbf{q}_1 \\
\mathbf{q}_3 &= \mathbf{T}(\alpha) \cdot \mathbf{q}_2 = \mathbf{T}(2\alpha) \cdot \mathbf{q}_1 \\
&\vdots \quad\quad \vdots \\
\mathbf{q}_j &= \mathbf{T}[(j-1)\alpha] \cdot \mathbf{q}_1, \quad j = 2, 3, \cdots, n
\end{aligned} \tag{21}$$

The derivation of Eq. (21) takes into account the property of the complex transformation matrix $\mathbf{T}(\alpha)$ due to its particular structure as indicated by Eq. (12):

$$\mathbf{T}[(j-1)\alpha] = [\mathbf{T}(\alpha)]^{j-1} \tag{22}$$

where the superscript $(\cdot)^{j-1}$ denotes the $(j-1)^{\text{th}}$ power of a matrix. And therefore $\mathbf{T}[(j-1)\alpha]$ can be readily computed in accordance with $\mathbf{T}(\alpha)$.

The SMART reduction mode basis is eventually formulated in the sector level by assembling the cyclic mode basis for each individual sector $\bar{\mathbf{\Phi}}_j^{\mathrm{IMT}}$ from 1 to n:

$$\bar{\mathbf{x}} = \begin{bmatrix} \bar{\mathbf{x}}_1 \\ \vdots \\ \bar{\mathbf{x}}_j \end{bmatrix} = \begin{bmatrix} \bar{\mathbf{\Phi}}_1^{\mathrm{IMT}} \cdot \mathbf{q}_1 \\ \vdots \\ \bar{\mathbf{\Phi}}_j^{\mathrm{IMT}} \cdot \mathbf{q}_j \end{bmatrix} = \begin{bmatrix} \bar{\mathbf{\Phi}}_1^{\mathrm{IMT}} \\ \vdots \\ \bar{\mathbf{\Phi}}_j^{\mathrm{IMT}} \cdot \mathbf{T}[(j-1)\alpha] \end{bmatrix} \cdot \mathbf{q}_1 = \bar{\mathbf{\Phi}}^{\mathrm{SMART}} \cdot \mathbf{q}_1, \quad j = 2, 3, \cdots, n \tag{23}$$

Note that Eq. 21 resulted from the enforced displacement compatibility condition is utilized to condense the

dependent modal coordinates $\mathbf{q}_j$. As a consequence, $\mathbf{q}_1$ becomes the one and only retained generalized coordinates. The sector-level modes at the jth sector is updated once again as $\bar{\mathbf{\Phi}}_j^{\text{IMT}} \cdot \mathbf{T}[(j-1)\alpha]$ in the assembled mode basis $\bar{\mathbf{\Phi}}^{\text{SMART}}$. This implies that each sector has basically identical modal deflection at the disk interface DOFs, nevertheless, with an inter-sector phase difference denoted by $\mathbf{T}(\alpha)$. It can be further inferred that the disk mode shapes involved in $\bar{\mathbf{\Phi}}^{\text{SMART}}$ are highly close to the mode shapes of a disk with perfect cyclic symmetry. In fact, the SMART approach attempts to approximate the full blisk vibration by the assembled sector mode basis carrying "almost" cyclic symmetric disk modal information. Meanwhile, the characteristic blade mode information of each sector with a unique blade geometry is completely preserved in the SMART mode basis.

Substituting $\bar{\mathbf{\Phi}}^{\text{SMART}}$ into Eq. 10 yields the reduced system quantities of the SMART ROM. In the implementation practice, only the real part of the SMART mode basis is retained during the sector-level computations.

C. Discussions

The complete process of constructing the SMART mode basis is conceptually illustrated in Fig. 2. On top of this schematic diagram, features and advantages of the SMART approach are briefly summarized and discussed below.

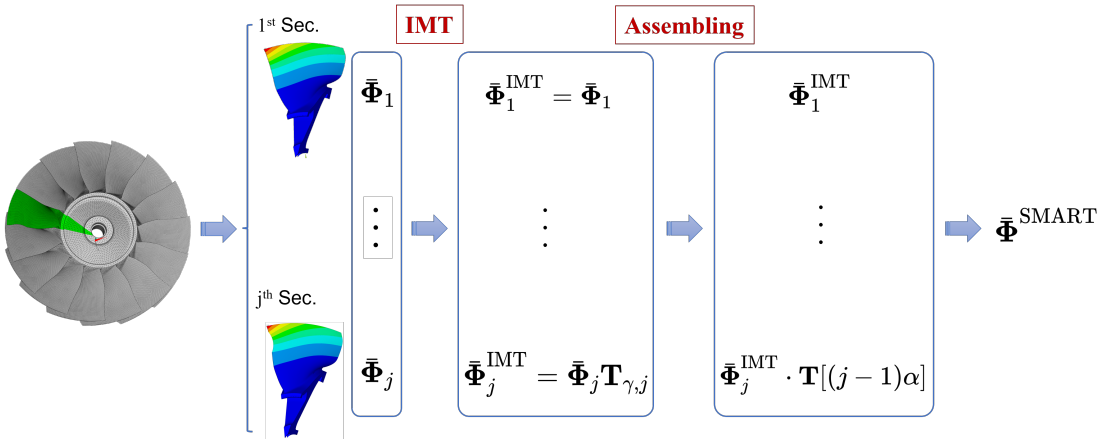

Fig. 2 Schematic diagram of the SMART mode basis construction process

- Wide applicability. As shown in Fig. 2, the SMART approach starts from partitioning the full-order blisk FEM into *n* "isolated" sectors and the cyclic modes associated with each individual sector are proceeded independently, making each sector analysis more computationally efficient with moderate memory usage compared to the full blisk computation. Note that the computational gains due to the lowered memory requirement are especially appreciable for high fidelity blisk models of huge size. Moreover this procedure of substructuring steps brings two-fold benefits. On the one hand, the SMART approach is able to cope with both small and large geometric mistuning occurring simultaneously within one blisk. In fact, each sector could have an incompatible blade mesh with respect to the other sectors. This is a great advantage in comparison with the existent system-mode-based

reduction methods, where the scope is confined to the small geometric mistuning with topological compatible meshes over all the blades [30]. On the other hand, the cyclic modes for each individual sector are strategically assembled into the SMART reduction mode basis with a block structure. This makes the SMART approach particularly suitable for evaluating the impacts of blade damages or blend repairs occurring in different shapes, sizes and locations within a specific blisk. In fact, in case of a newly damaged or repaired blade, instead of recalculating the whole reduction mode basis, the SMART merely requires to update the sector-level cyclic modes for the specific sector undergoing modifications in a straightforward manner.

- Simple implementation. The SMART mode basis is constructed by solely utilizing the cyclic modes truncated both modally and spatially, for each individual geometrically mistuned sector. Moreover, the column vectors in $\bar{\mathbf{\Phi}}_j^{\mathrm{SMART}}$ stemmed from these cyclic modes inherently remain linearly independent. Hence, the implementation of the SMART approach is rather simple. As indicated in Fig. 2, the independently processed cyclic modal analyses for all the individual sectors constitute the substantial offline cost of the SMART approach. Then the interface mode transformation and the sector mode assembling process are realized at a negligible computational cost. It must be observed that the aforementioned component-mode-based reduction methods in literature incorporate the constraint modes of each sector into the projection basis [23]. For industrial blisk FEMs with a large number of interface DOFs, the computation of constraints modes is cumbersome or even quite prohibitive.
- High reduction performance. The reduction mode basis $\bar{\mathbf{\Phi}}^{\mathrm{SMART}}$ has a size of n_m in the column dimension, which is the number of retained cyclic modes for a single sector. This produces a minimal size of the SMART ROM that is able to effectively represent the full-order blisk dynamics with n_m modes. By comparison, the system-mode-based reduction methods in literature, employ an expanded projection basis by incorporating more sets of cyclic modes for different geometrically mistuned sector types. Accordingly, the projection basis size in the column dimension becomes $n_m \times n_s$, provided that the total number of different geometrically mistuned sector types is n_s and n_m cyclic modes are retained for each sector type, respectively [28]. While the ROMs derived by the component-mode-based reduction methods in literature are generally of even larger size since the interface DOFs of each sector are partly preserved [26, 27].

III. Results

In this section, the SMART approach will be applied into an "As-Measured Model", namely, a high-fidelity blisk FEM of a blended blisk, built upon the measurement of the true blisk geometry through a 3D optical scanning technology. The SMART ROM will be constructed to compute both the natural frequencies and mode shapes, as well as the forced responses of the blisks under typical engine order excitations. These reduced-order model results will be validated against the full-order blisk model analysis results obtained in ANSYS®.

A. As-Measured Model of a Blend Blisk

This subsection presents an "As-Measured Model" (AMM) of a blended blisk test piece, built upon the measured geometry by a non-contact ATOS structured-blue-light 3D scanner. The blisk test piece specifically manufactured for academic research, consists of $n = 15$ downscaled, low-aspect-ratio blades on a disk with simplified geometry. The blade 7 is purposefully blended as shown in Fig. 3(a). The AMM intends to accurately model the variances of blade frequencies and mode shapes within the real blisk in the presence of both the blend repair and small intrinsic geometry mistuning due to manufacturing tolerances, etc. The methodologies of constructing the AMM will be briefly revisited hereafter. For complete details, readers are referred to the authors' recent research work [15].

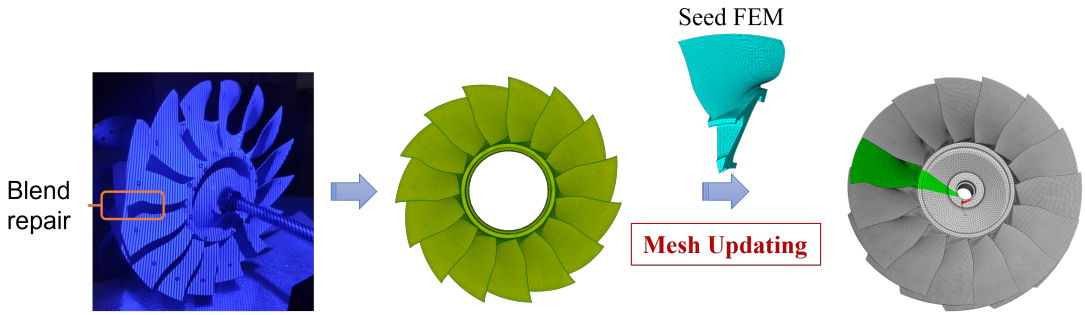

(a) Fringe projection scan (b) Blisk point cloud (c) As-Measured Model

Fig. 3 Construction of the As-Measured Model.

The geometry measurement by the ATOS optical scanner basically includes a number of fringe projection scans that precisely acquire all the blade surface geometry shape data in the form of point cloud with very high resolutions. The blisk point cloud is then post-processed and converted into a highly dense, triangulated surface mesh as depicted in Fig. 3(b). Since the blade-to-blade geometry variances are of major concern, the disk part inside the rim is not included in the point cloud.

In general, the AMM is constructed by updating the blade surface mesh of an existing "seed" FEM in order to better match the blisk point cloud representing the measured geometry of the real one-piece component. A seed FEM refers to a full blisk model with quadratic tetrahedral elements, usually coming from a nominal blisk design, which serves as an initial approximation of the real component with blade geometry variations. More specifically, the mesh updating strategy is illustrated in Fig. 4 and it aims to project each individual surface node $N(x, y, z)$ of the seed FEM along the vector $\vec{h}$, onto the plane determined by its 3 nearest neighboring vertices (v_1, v_2, v_3) in the point cloud. As a consequence, the surface mesh of the FEM can be updated with the modified node coordinates $N'(x', y', z')$ after the node projection procedure and the interior volume mesh will be regenerated accordingly.

The mesh updating strategy in the basic form works smoothly provided that the FEM to PC (point cloud) distance is small, as indicated by the projection of node N_1 in the upper part of Fig. 4. However, technical difficulty commonly

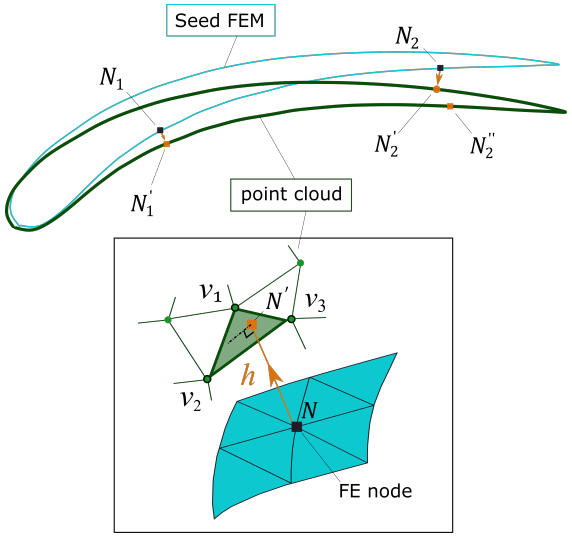

Fig. 4 Mesh updating strategy.

arises for the large-sized blades experiencing geometric variations of relatively high magnitude. For instance, Fig. 4 depicts the potential projection problem of node N_2 near the trailing edge tip, where the local blade deformation exceeds the local blade thickness. By following the original mesh updating scheme, the seed FEM node N_2 on the pressure side will be automatically translated onto the closest point cloud on the suction side as an incorrect projected node N_2', whereas N_2'' should be the correct node projection on the pressure side of the blade point cloud.

An improved mesh updating strategy incorporating a "pre-morphing" step is therefore proposed by the authors in Ref.[15] in order to override the potential problem of spurious node projection. As shown in Fig. 5, the seed FEM node N_1 in the reference surface is firstly projected to its closest point cloud along the deformation vector $\vec{h}_1^{\text{pre}}$ as N_1^{pre}. The reference surface refers to one of the blade surfaces in the seed FEM, i.e., either the suction side or the pressure side, that practically deviates more from the blade PC. Then the nearest neighboring node of N_1 among the seed FEM blade surface nodes other than the reference surface, denoted by N_2, is also pre-morphed as N_2^{pre} by imposing the same deformation vector $\vec{h}_1^{\text{pre}}$. Since the pre-morphed nodes N_i^{pre} approach the blade point cloud more than before, they will be translated to the correct position onto the point cloud by the node projection procedure depicted in Fig. 4.

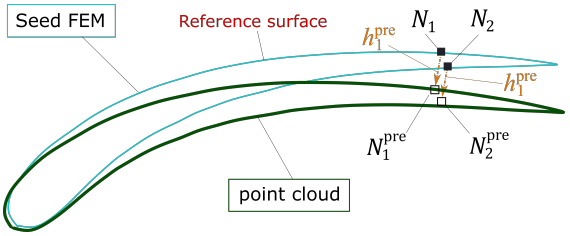

Fig. 5 Pre-morphing step of the improved mesh updating strategy.

The improved mesh updating strategy was proved well suited to the AMM construction for large-sized blades

experiencing geometric variations of high magnitude. Note that for the blended sector, a seed FEM built upon a nominal blade with an approximated standard blend shape and geometry is recommended. Otherwise, the updated FEM mesh could become warped or inverted around the blend. The resultant AMM in Fig. 3(c) is able to fully capture the measured blade-to-blade geometry variances with high-fidelity. It further allows to directly evaluate the mth blade-alone frequency (cantilevered blade frequency) mistuning pattern ${}^{f}\delta_{m,i}$ due to geometric mistuning as

$$ {}^{f}\delta_{m,j} = \frac{f_{m,j} - \bar{f}_m}{\bar{f}_m}, \quad j = 1, 2, \cdots, n \tag{24} $$

where the preceding superscript ${}^{f}(\cdot)$ stands for the frequency mistuning; $f_{m,j}$ denotes the mth cantilevered blade modal frequencies of the jth blade; $\bar{f}_m$ is the mean value of the blade modal frequencies $f_{m,j}$ for $j = 1, \cdots, n$.

The computed blade-alone frequency mistuning patterns are plotted in Fig. 6. It can be seen that the blade geometric variances affect the blade-alone frequency mistuning patterns to different extents. For the first bending (1B) blade mode, frequency mistuning magnitudes of most blades fall into a narrow band, including the blended blade 7. The only exception comes from the blade 15 with a high frequency mistuning value up to 1.79%. The reason is that the blisk test piece is made of aluminium and before the optical scanning, an unexpected geometric deflection in the tip area occurred during delivery process, which is detectable by visual inspection. For the first torsional (1T) blade mode, the frequency mistuning values scatter in a wider range. Apart from the blade 15, appreciable frequency variations are also observed at the blade 1 and 13. It is thus inferred that the 1T blade mode is more sensitive to the blade geometry variations than the 1B blade mode.

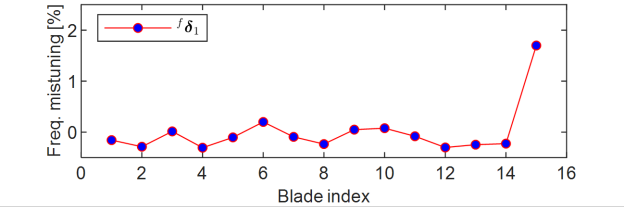

(a) 1B mode

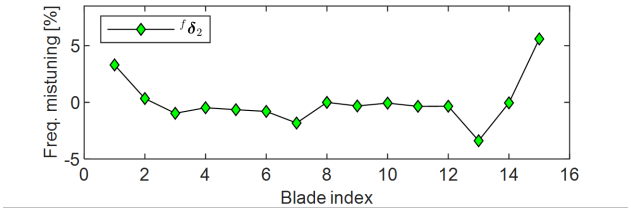

(b) 1T mode

Fig. 6 Frequency mistuning patterns evaluated by AMM.

In the previous paper [15] the authors have demonstrated that the AMM is able to capture not only the 'blade-alone'

frequency and mode shape variations due to both the blend and intrinsic blade geometry variances, but also the global dynamics of the blended blisk with acceptable accuracy. For the sake of brevity, this topic is not covered in this paper.

B. SMART ROM construction

The SMART approach presented in Sec.II is applied to the AMM of the blended blisk. Clamping boundary conditions are imposed to constraint the DOFs at the hub of the blisk. The AMM consists of around 3.67×10^6 quadratic tetrahedral elements with approximately 5.71×10^6 nodes. The huge AMM size drives the requirement of large amounts of physical memory. The full-order AMM is therefore simulated on a workstation with 10 cores @1.9 GHz and 64 GB of memory. It should be pointed out that for large scale model simulations, maximum computational performance generally occurs only when there is sufficient physical memory to comfortably run the equation solver while also caching the large files generated during the simulation. Hence, the achievable computation performance on this given machine is still limited because in fact more than 90% memory usage is dedicated to solving the large system equations.

The SMART approach is initiated by the cyclic modal analysis independently performed on each individual sector of the AMM with assumed cyclic symmetry at the sector interfaces. A remarkable advantage of the SMART approach is that the sector-level cyclic modal analysis is carried out with much lower memory usage, in contrast to the full-order AMM analysis. Each cyclic modal analysis enables to generate a Frequency-Nodal Diameter (ND) plot for the designated sector. For example, the Frequency-ND plots for the 1st (the reference sector for the IMT) and 7th sector (with blend repair) respectively, are superimposed in Fig. 7. Appreciable frequency deviations, arising from the distinct blade geometries in the two sectors, can be observed over almost all the mode families.

It is well known that the accuracy of ROM is largely dependent on the number of modes retained in a specified frequency range in the reduction basis. In this research, the target frequency range is set roughly below 1600Hz such that the 1B and 1T modal family of the AMM can be fully covered. Within this target frequency range, a selected collection of $n_m = 35$ cyclic modes $\bar{\mathbf{\Phi}}_j$ are retained for the sector-level mode projection presented in Eq. (11). As visible in Fig. 7, this projection basis contains the 30 cyclic modes of the 1B and 1T modal families, as well as the 5 cyclic modes corresponding to the 3rd modal family at 0~2ND, for each individual sector of the AMM. The latter are included due to the fact that the modal frequencies and deformed blade shapes of these cyclic modes, are very close to that of the blade-dominant modes with high nodal diameters (3~7ND) in the 1T modal family. As a consequence, it gives rise to the SMART ROM of the size $n_m = 35$. It will be demonstrated later on that the adequate system modal information involved in this reduction mode basis enables the SMART ROM to accurately reproduce the full-order blisk dynamics in the frequency range around the 1B and 1T modal families.

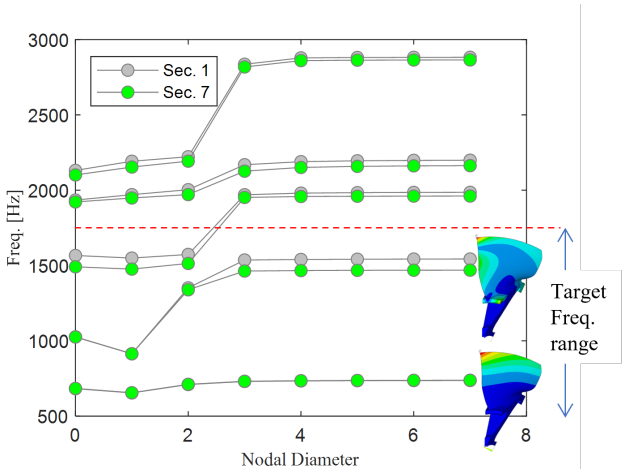

Fig. 7 Frequency-Nodal Diameter plots.

C. Modal properties

The reduced quantities presented in Eq. (3) allow to compute $n_m = 35$ natural frequencies of the SMART ROM. Meanwhile, the first 35 natural frequencies of the full-order blisk FEM are obtained by performing a modal analysis for the AMM in ANSYS®. The blisk natural frequencies derived by the AMM and SMART ROM respectively, are compared in Fig. 8 and the relative estimation error pertained to each blisk mode is also quantified to evaluate the accuracy of the SMART ROM. The relative estimation error is defined as $\left(f_j^{\text{SMART}} - f_j^{\text{AMM}}\right)/f_j^{\text{AMM}}$ where f_j^{AMM} is the jth frequency calculated by the AMM for $j = 1, 2, \cdots, n_m$ and f_j^{SMART} is the counterpart computed by the SMART ROM. It can be immediately seen that the natural frequencies predicted by the SMART ROM almost perfectly match that of the full-order AMM. The relative errors are extremely low, roughly below 0.05%.

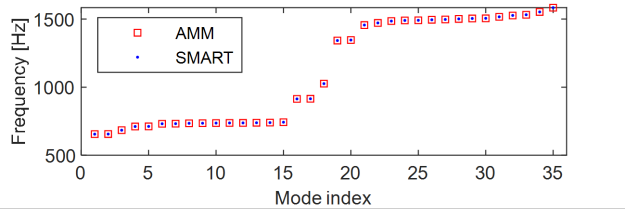

(a) Natural frequency

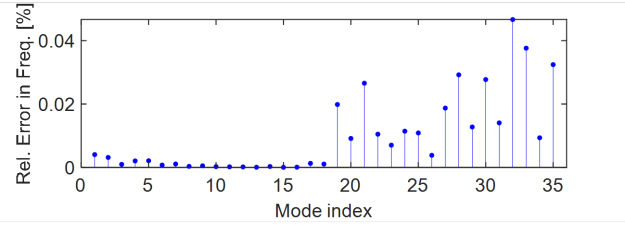

(b) Relative error in frequency

Fig. 8 Comparison of natural frequencies evaluated by AMM and SMART ROM.

Moreover, both the AMM and SMART ROM enable to construct the representative blisk mode shapes by extracting the modal amplitudes in the axial direction (UZ) at the same node around each blade leading edge tip. Typical blisk mode shapes are compared in the normalized form, as depicted in Fig. 9. The blisk mode shape (mode index = 14) in Fig. 9(a) is characterized as intermediately localized, since several blades exhibit relatively high modal amplitudes, but still there is an obvious dominance by the three blades (7 ~ 9). Fig. 9(b) presents an almost sinusoidal blisk mode shape (mode index = 20) and the 2 nodal diameters can be clearly identified. Overall, Fig. 9 shows excellent agreement between the AMM and SMART ROM results for both the two sets of blisk modes. Hence, the capability of the SMART ROM in reproducing the modal properties of the AMM with high accuracy is fully demonstrated.

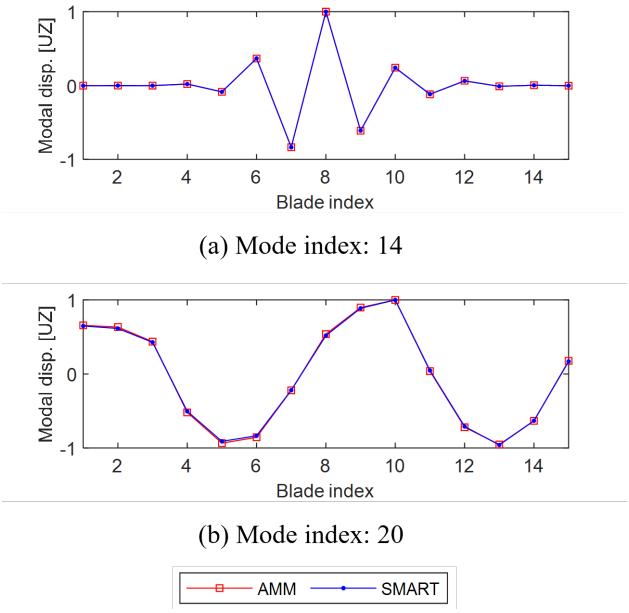

(a) Mode index: 14

(b) Mode index: 20

Fig. 9 Comparison of blisk mode shapes evaluated by AMM and SMART ROM.

D. Forced responses

The forced responses of the blended blisk under typical engine-order (EO) excitation are assessed by the AMM and SMART ROM, respectively. For the purpose of verifying the accuracy of the SMART ROM, an arbitrarily chosen EO = 5 excitation is imposed on the blisk. This represents a high engine-order excitation that tends to excite the blade-dominant vibration in the blisk. Specifically, it is composed of n unit nodal forces simultaneously applied in the axial direction at the same specified position of each blade. The unit nodal forces are harmonic in time and differ only in phase from blade to blade. A very low structural damping ratio $\gamma = 0.0005$ is assigned for the forced response calculations.

The forced response curves in the axial direction (UZ) at the leading edge tip of the blended blade 7 are closely examined in Fig. 10. As revealed in the previous subsection, a certain number of blisk mode shapes are no longer

pure nodal diameter modes, but instead could be decomposed into multiple harmonic contents. Even though the blisk undergoes a single engine-order excitation, those blisk modes that retain significant harmonic contents matching the engine order of the excitation can be strongly excited. As a result, it can be seen in Fig. 10 that several response peaks amplitudes arise in the frequency range around the 1B and 1T mode family. The forced response curves derived from the reduced-order model by SMART show close-to-perfect match with the counterparts directly computed by the AMM, both in terms of peak frequencies and amplitudes. This demonstrates the reliability of SMART in reproducing the forced responses of the full-order as-measured blisk model.

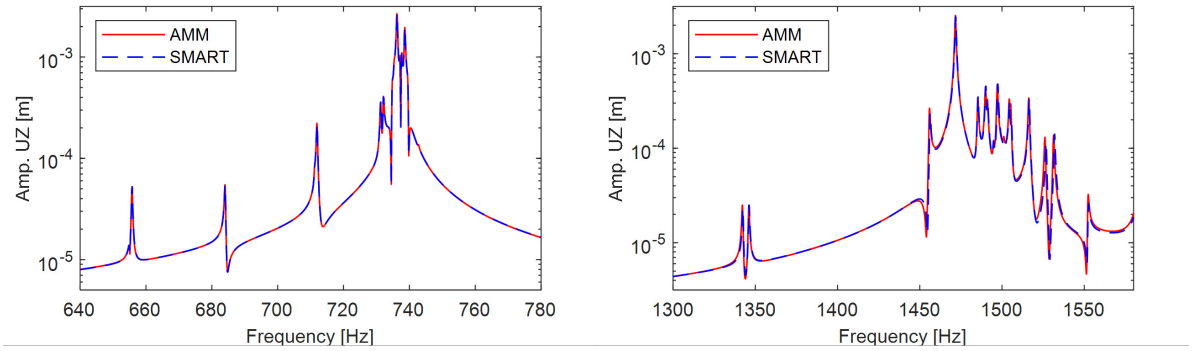

(a) Around 1B mode family

(b) Around 1T mode family

Fig. 10 Comparison of forced responses at blade 7 evaluated by AMM and SMART ROM.

IV. Conclusion

This paper presents an original model reduction technique, the SMART approach, specifically for the blisks fully mistuned by blade geometric variations, with either topologically compatible or incompatible blade meshes. Namely, the blades experiencing large geometric modification do not necessarily have substantially similar topology and exactly the same FE node numbers with the nominal blade.

In principle, this approach constructs the sector-level reduction mode basis by using only the truncated cyclic modes computed independently for each "isolated" sector, assuming cyclic symmetry at the sector interfaces. This leads to a huge reduction of memory consumption compared with the full-order blisk model computation. The key point of SMART is that the mode basis completely preserves the mode information pertained to each blade given by its specific geometric configuration, while the underlying disk is treated as cyclic symmetric. Due to the particular block structure of the SMART mode basis, the reduced-order blisk model can be obtained by means of a series of sector-level computations with a relatively low memory requirement and computational cost. Moreover, the SMART approach can be potentially very efficient in case that the reduced model needs to be updated for structural modifications of one or more blades. In this situation, only the sectors undergoing blade modifications needs to be re-evaluated and their modes will be replaced in the the SMART mode basis.

In the present paper, effectiveness of the SMART approach was successfully verified by its application to the high fidelity As-Measured Model of a blended blisk constructed on the true geometry acquired by the state-of-the-art 3D optical scanning technology. It was demonstrated that the reduced-order model by SMART is capable of reproducing the dynamics of the full-order as-measured blisk model with high accuracy.

The SMART approach could be considered a viable and valuable numerical tool in the frame of the digital twin philosophy throughout the blisk's life-cycle. On the one hand, the huge-sized, physics-based blisk models converted directly from the precise geometry measurement data naturally need an efficient and accurate model reduction technique such as SMART. On the other hand, the SMART approach is particularly suitable for updating the blisk model by detecting the real blade geometry evolving in the service life, with low computational effort. This research is therefore in accordance with the goal of leveraging the leading-edge digital technology across the turbomachinery industry.

Funding Sources

This work has received funding from the European Union's Horizon 2020 research and innovation program under the Marie Sklodowska-Curie grant agreement No. 891197. This work is also part of a project that has received funding from National Natural Science Foundation of China (Grant No. 52175098). This support is also gratefully acknowledged.

References

[1] Ganine, V., Legrand, M., Michalska, H., and Pierre, C., "A sparse preconditioned iterative method for vibration analysis of geometrically mistuned bladed disks," *Computers & Structures*, Vol. 87, No. 5, 2009, pp. 342–354.

[2] Mbaye, M., Soize, C., Ousty, J.-P., and Capiez-Lernout, E., "Robust Analysis of Design in Vibration of Turbomachines," *Journal of Turbomachinery*, Vol. 135, No. 2, 2012.

[3] Schnell, R., Lengyel-Kampmann, T., and Nicke, E., "On the Impact of Geometric Variability on Fan Aerodynamic Performance, Unsteady Blade Row Interaction, and Its Mechanical Characteristics," *Journal of Turbomachinery*, Vol. 136, No. 9, 2014, pp. 091005–091005–14.

[4] Vishwakarma, V., and Sinha, A., "Forced Response Statistics of a Bladed Rotor with Geometric Mistuning," *AIAA Journal*, Vol. 53, No. 9, 2015, pp. 2776–2781.

[5] Kaszynski, A. A., Beck, J. A., and Brown, J. M., "Automated Finite Element Model Mesh Updating Scheme Applicable to Mistuning Analysis," *Proceedings of ASME Turbo Expo 2014*, Düsseldorf, Germany, 2014, p. V07BT33A025.

[6] Backhaus, T., Maywald, T., Schrape, S., Voigt, M., and Mailach, R., "A Parametrization Describing Blisk Airfoil Variations Referring to Modal Analysis," *Turbomachinery Technical Conference and Exposition*, Vol. Structures and Dynamics, Charlotte, NC, USA, 2017, p. V07AT32A003.

[7] Meckstroth, C., and Brown, J., "Point Cloud to Parameter: An Inverse Geometric Approach to Probabilistic Design," *ASME Turbo Expo 2019: Turbomachinery Technical Conference and Exposition*, Vol. Volume 7A: Structures and Dynamics, Phoenix, Arizona, USA, 2019.

[8] Maywald, T., Backhaus, T., Schrape, S., and Kühhorn, A., "Geometric Model Update of Blisks and its Experimental Validation for a Wide Frequency Range," *ASME Turbo Expo 2017: Turbomachinery Technical Conference and Exposition*, Charlotte, North Carolina, USA, 2017, p. V07AT30A001.

[9] Kaszynski, A. A., Beck, J. A., and Brown, J. M., "Automated Meshing Algorithm for Generating As-Manufactured Finite Element Models Directly From As-Measured Fan Blades and Integrally Bladed Disks," *Turbomachinery Technical Conference and Exposition GT2018*, Vol. Structures and Dynamics, Oslo, Norway, 2018, p. V07CT35A024.

[10] Gillaugh, D. L., Kaszynski, A. A., Brown, J. M., Beck, J. A., and Slater, J. C., "Mistuning Evaluation Comparison Via As-Manufactured Models, Traveling Wave Excitation, and Compressor Rigs," *Journal of Engineering for Gas Turbines and Power*, Vol. 141, No. 6, 2019.

[11] Kaszynski, A. A., and Brown, J. M., "Accurate Blade Tip Timing Limits Through Geometry Mistuning Modeling," *Turbine Technical Conference and Exposition*, Montréal, Canada, 2015, p. V07AT27A007.

[12] Beck, J. A., Kaszynski, A. A., Brown, J. M., Gillaugh, D. L., and Scott-Emuakpor, O. E., "Selection of Dynamic Testing Measurement Locations for Integrally Bladed Disks," *Turbomachinery Technical Conference and Exposition GT2018*, Vol. Structures and Dynamics, Oslo, Norway, 2018, p. V07CT35A037.

[13] Gambitta, M., Kühhorn, A., and Schrape, S., "Geometrical Variability Modelling of Axial Compressor Blisk Aerofoils and Evaluation of Impact on the Forced Response Problem," *Turbo Expo: Power for Land, Sea, and Air*, Vol. 84096, American Society of Mechanical Engineers, 2020, p. V02DT38A028.

[14] Brown, J., Kaszynski, A., Gillaugh, D., Carper, E., and Beck, J., "Optimization of Airfoil Blend Limits with As-manufactured Geometry Finite Element Models," *Journal of Engineering for Gas Turbines and Power*, 2021.

[15] Zhou, B., Zhao, J., Ye, N., and Berruti, T. M., "Blisk with small geometric mistuning and blend repair: As-Measured Model and Experimental Verification," *Turbo Expo: Power for Land, Sea, and Air*, Vol. In publication, American Society of Mechanical Engineers, 2022.

[16] Kaszynski, A. A., Beck, J. A., and Brown, J. M., "Experimental Validation of a Mesh Quality Optimized Morphed Geometric Mistuning Model," *ASME Turbo Expo 2015: Turbomachinery Technical Conference and Exposition*, Montréal, Canada, 2015, p. V07AT27A005.

[17] Salas, M. G., Bladh, R., Mårtensson, H., Petrie-Repar, P., Fransson, T., and Vogt, D. M., "Forced Response Analysis of a Mistuned, Compressor Blisk Comparing Three Different Reduced Order Model Approaches," *Journal of Engineering for Gas Turbines and Power*, Vol. 139, No. 6, 2017.

[18] Tang, W., Epureanu, B. I., and Filippi, S., "Models for blisks with large blends and small mistuning," *Mechanical Systems and Signal Processing*, Vol. 87, 2017, pp. 161–179.

[19] Gan, Y., Mayer, J. L., D'Souza, K. X., and Epureanu, B. I., "A Mode-Accelerated XXr (MAX) method for complex structures with large blends," *Mechanical Systems and Signal Processing*, Vol. 93, 2017, pp. 1–15.

[20] Gao, J., Gao, Y., Yan, X., Xu, K., and Sun, W., "Reduced Order Models for Largely Mistuned Blisks with Small Random Mistuning," *AIAA Journal*, Vol. 58, No. 6, 2020, pp. 2691–2701.

[21] Schwerdt, L., Panning-von Scheidt, L., and Wallaschek, J., "A Model Reduction Method for Bladed Disks With Large Geometric Mistuning Using a Partially Reduced Intermediate System Model," *Journal of Engineering for Gas Turbines and Power*, Vol. 143, No. 7, 2021.

[22] Beck, J. A., Brown, J. M., Cross, C. J., and Slater, J. C., "Component-Mode Reduced-Order Models for Geometric Mistuning of Integrally Bladed Rotors," *AIAA Journal*, Vol. 52, No. 7, 2014, pp. 1345–1356.

[23] Beck, J. A., Brown, J. M., Kaszynski, A. A., Carper, E. B., and Gillaugh, D. L., "Geometric Mistuning Reduced-Order Model Development Utilizing Bayesian Surrogate Models for Component Mode Calculations," *Journal of Engineering for Gas Turbines and Power*, Vol. 141, No. 10, 2019.

[24] Beck, J. A., Brown, J. M., Kaszynski, A. A., and Gillaugh, D. L., "Numerical Methods for Calculating Component Modes for Geometric Mistuning Reduced-Order Models," *Journal of Engineering for Gas Turbines and Power*, Vol. 144, No. 3, 2021.

[25] Beck, J. A., Brown, J. M., Runyon, B., and Scott-Emuakpor, O. E., "Probabilistic Study of Integrally Bladed Rotor Blends using Geometric Mistuning Models," *58th AIAA/ASCE/AHS/ASC Structures, Structural Dynamics, and Materials Conference*, Grapevine, Texas, US, 2017.

[26] Beck, J. A., Brown, J. M., Kaszynski, A. A., Cross, C. J., and Slater, J. C., "Geometric Mistuning Reduced-Order Models for Integrally Bladed Rotors With Mistuned Disk-Blade Boundaries," *Journal of Turbomachinery*, Vol. 137, No. 7, 2015, p. 071001.

[27] Carassale, L., Cavicchi, A., Bruzzone, S., and Marrè Brunenghi, M., "Probabilistic Response of a Bladed Disk With Uncertain Geometry," *Journal of Engineering for Gas Turbines and Power*, Vol. 141, No. 10, 2019.

[28] Mbaye, M., Soize, C., and Ousty, J.-P., "A reduced-order model of detuned cyclic dynamical systems with geometric modifications using a basis of cyclic modes," *Journal of engineering for gas turbines and power*, Vol. 132, No. 11, 2010.

[29] Vishwakarma, V., Sinha, A., Bhartiya, Y., and Brown, J. M., "Modified Modal Domain Analysis of a Bladed Rotor Using Coordinate Measurement Machine Data on Geometric Mistuning," *Journal of Engineering for Gas Turbines and Power*, Vol. 137, No. 4, 2015, pp. 042502–042502–8.

[30] Baek, S., and Epureanu, B., "Reduced-Order Models of Blisks With Small Geometric Mistuning," *Journal of Vibration and Acoustics*, Vol. 139, No. 4, 2017, pp. 041003–041003–10.

[31] Lupini, A., and Epureanu, B. I., "On the use of mesh morphing techniques in reduced order models for the structural dynamics of geometrically mistuned blisks," *Mechanical Systems and Signal Processing*, Vol. 127, 2019, pp. 262–275.